Available online at www.sciencedirect.com

SCIENCE DIRECT®

Journal of Catalysis 239 (2006) 451–459

JOURNAL OF CATALYSIS

www.elsevier.com/locate/jcat

Bifunctional catalytic isomerization of decane over MTT-type aluminosilicate zeolite crystals with siliceous rim

Ward Huybrechts [a], Joris W. Thybaut [d], Bart R. De Waele [a], Gina Vanbutsele [a], Kristof J. Houthoofd [a], Fabrice Bertinchamps [b], Joeri F.M. Denayer [c], Eric M. Gaigneaux [b], Guy B. Marin [d], Gino V. Baron [c], Pierre A. Jacobs [a], Johan A. Martens [a,*]

[a] *Centrum voor Oppervlaktechemie en Katalyse, Katholieke Universiteit Leuven, Kasteelpark Arenberg 23, B-3001 Leuven, Belgium*
[b] *Unité de Catalyse et Chimie des Matériaux Divisés, Université Catholique Louvain, Croix du Sud, 2 Bte 17, B-1348 Louvain-la-Neuve, Belgium*
[c] *Dienst Chemische Ingenieurstechniek, Vrije Universiteit Brussel, Pleinlaan 2, B-1050 Brussel, Belgium*
[d] *Laboratorium voor Petrochemische Techniek, Universiteit Gent, Krijgslaan 281 S5, B-9000 Gent, Belgium*

Received 8 July 2005; revised 15 February 2006; accepted 26 February 2006

Abstract

Micrometer-size MTT-type zeolite crystals with aluminum depletion in the outer layer were synthesized. The compositional variation in individual crystals was obtained by altering the chemical composition of the gel during crystal growth of MTT-type zeolite. Chemical composition of the bulk and the surface of the crystals was determined using ^{27}Al MAS NMR and XPS, respectively. The zeolite with siliceous rim was converted into a bifunctional catalyst by neutralizing the cation-exchange capacity with protons and plating with a trace amount of platinum metal. The MTT zeolite with siliceous crystal termination was catalytically much less active than the isostructural ZSM-23 zeolite with homogeneous chemical composition. The catalytic activity reflects the aluminum content on the surface of the crystals determined by XPS, rather than the bulk composition. The reaction mechanism and the reaction kinetics were analyzed using a microkinetic model developed previously for the structurally related TON-type zeolite. The catalytic data are in favor of the pore mouth catalysis model of skeletal isomerization of long n-alkanes on 10-membered ring tubular pore zeolites.

Keywords: ZSM-23 zeolite; Compositional gradient; Decane isomerization; Pore-mouth catalysis; Isodewaxing; Single-event microkinetics

1. Introduction

Catalytic conversion processes of long n-alkanes over bifunctional zeolites with 10-membered ring (10-MR) pore systems have been applied in several petroleum refining processes related to the manufacturing of diesel fuel, aviation fuel, and lubricants [1]. Zeolites with 10-MR monodimensional pore systems, such as in the framework topologies TON, MTT and AEL, limit cracking during skeletal isomerization of long n-alkanes. Investigations of the skeletal branching of n-alkanes on bifunctional 10-MR zeolites has produced several explanations for the unique properties of these 10-MR zeolites, including transition state shape selectivity [2,3] diffusion selectivity [4,5], and pore mouth and key–lock catalysis [6]. According to the latter explanation, the reacting hydrocarbon molecule is adsorbed partly inside the pore and partly on the external surface of the zeolite crystal. Distinction between pore mouth and key–lock catalysis is based on the penetration of the molecule into one or two pore mouths, respectively [6]. Short alkanes, such as octane, are converted mainly via pore mouth catalysis [7]. Longer molecules can bridge the distance between adjacent micropore openings and react via the key–lock mechanism on bridge acid sites at the external surface, in addition to pore mouth catalysis [8]. Side chains are generated in that part of the hydrocarbon chain lying on the outside of the first 10-MR along the pore. A fundamental kinetic model based on pore mouth and key–lock catalysis has been developed and successfully implemented for the description of hydroconversion

---

[*] Corresponding author. Fax: +32 16 321998.
E-mail address: johan.martens@biw.kuleuven.be (J.A. Martens).

0021-9517/$ – see front matter © 2006 Elsevier Inc. All rights reserved.
doi:10.1016/j.jcat.2006.02.020

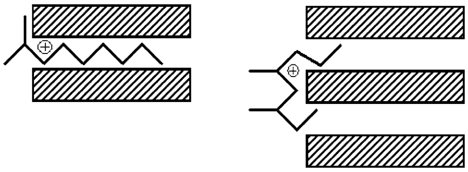

Fig. 1. Examples of alkylcarbenium ions in a pore mouth and on a bridge between pore mouths. Left: 2-methyl-non-3-yl cation in pore mouth; right: 3,5-dimethyl-oct-5-yl cation on a bridge.

of n-alkanes on Pt/H-ZSM-22 [7,8]. In bifunctional catalysis, hydrocarbons are converted into alkylcarbenium ion intermediates on protonation of alkenes formed by dehydrogenation on the noble metal. The alkylcarbenium ions undergo skeletal rearrangement and cracking via β-scission. In pore mouth catalysis, due to sterical hindrance, the reaction network is restricted to secondary alkylcarbenium ions (Fig. 1). In addition, geminal dibranching, ethylbranching, and alkyl shifts are excluded [7]. On bridge acid sites, no sterical hindrance is assumed in the kinetic model. In particular, conversions involving tertiary alkylcarbenium ions can occur (Fig. 1). Iso-alkanes have a low tendency toward cracking for several reasons. First, there is wide spreading of the branching positions along the main hydrocarbon chain of the preferred isomers, which is unfavorable for cracking through β-scission. Second, in pores and pore mouths, β-scission via secondary and primary alkylcarbenium ions involves high-energy barriers [7,8]. Third, physisorption and protonation stabilization is more pronounced at pore mouths than at bridge sites. Adsorption measurements [9–11], skeletal isomer distributions obtained with C_8–C_{24} n-alkanes [6,12,13], and rival kinetic model screening [14] all provide arguments in favor of the pore mouth catalysis model.

In the classic vision of shape-selective catalysis with zeolites, shape selectivity is linked to steric effects inside the zeolite micropores [15,16]. Active sites in pore mouths and on the external surfaces of zeolite crystals with less confinement are considered less selective than intracrystalline sites. The classic shape-selectivity concepts hold for relatively small molecules reacting via bulky reaction intermediates or transition states [17]. In that case, selectivity of the zeolite can be obtained by eliminating the external catalytic sites. For large molecules that do not penetrate deep into the crystals, pore mouths and "nests" on the external surface present reactive environments that can impose steric limitations [18,19]. According to the pore mouth catalysis model, active sites contributing catalytic turnovers are located in a shallow outer layer of the zeolite crystals with a thickness on the order of 1 nm. Zeolite crystals depleted with acid sites in this rim are expected to be inactive.

Various methods have been developed for eliminating active sites from zeolite crystal surfaces. This approach was applied successfully in the area of, for example, alkene oligomerization on acid zeolites [20,21]. In aluminosilicate zeolites, acidity is linked to the presence of Al atoms in the tetrahedral silicate framework. Selective dealumination of the external surface of zeolites can be achieved by reaction with $SiCl_4$, $(NH_4)_2SiF_6$, ethylenediaminetetraacetate, or oxalic acid [21–23]. Alternatively, the externally positioned acid sites can also be selectively poisoned by adsorption of bulky amines like collidine [24]. Another approach is to deposit a silica layer around the zeolite crystals via reaction with silicon alkoxides [21]. Beside deactivating the external surface, most of these treatments tend to deteriorate the porosity locally at the pore entrances, which often complicates interpretation of the reaction kinetics.

In zeolite synthesis, it is known that the aluminum distribution inside the zeolite crystals can be inhomogeneous. Al enrichment on the outer surface is most often encountered [25,26]. For eliminating the active sites from the zeolite crystal surface, a reverse zoning is desired. Li et al. [27] synthesized colloidal zoned MFI crystals in which a ZSM-5 core was covered with a Silicalite-1 shell and demonstrated the continuity of the overgrowth with SEM, TEM, and XPS. Samples with siliceous rim were shown to have considerably higher paraselectivity in the alkylation of toluene compared with a conventional ZSM-5-type catalyst [28].

In the area of bifunctional catalysis, selective dealumination of the external surface was attempted in one study [29]. Theta-1 zeolite (TON topology) was treated in aqueous HCl solution. Through this treatment, the bulk Si/Al atomic ratio of the zeolite determined by chemical analysis increased from 38 to 55. The concentration of acid sites, determined by titration with di-*tert*-butyl-pyridine, was decreased more strongly on the external surface of the dealuminated samples than on the bulk. The catalytic activity for hexadecane isomerization of parent and dealuminated samples was comparable despite the modification. This was explained by the improved accessibility of the acid sites of the zeolite by the treatment with HCl, as demonstrated by pyridine adsorption. Detailed reaction product analysis led the authors to conclude that an important part of the isomerization of hexadecane into 2- and 3-methylpentadecane occurred deep inside the pores of the Theta-1 zeolite, whereas the formation of centrally methylbranched skeletal isomers and dibranched isomers occurred mainly in pore mouths [29].

To verify the thesis of pore mouth catalysis in n-alkane isomerization, we synthesized MTT-type zeolites with pronounced Al depletion on the crystal surfaces. First, ZSM-23 crystal cores were grown from an aluminosilicate gel. The crystallization was continued by adding gel without aluminum and with an aluminum-sequestering agent, NH_4F. MTT zeolite samples with Al depletion in the rim and with homogeneous compositions were converted into bifunctional catalysts and evaluated in decane isomerization to evaluate the contribution of acid sites in the bulk and the pore mouths to catalytic activity.

2. Experimental

2.1. Materials

Hydrothermal zeolite synthesis was performed at 160 °C in 120-ml stainless steel autoclaves tumbling at ca. 60 rotations/min. The synthesis recipe of ZSM-23 was based on example 2 of Ref. [30]. Diquat-7 dibromide salt was prepared according to example A of Ref. [29]. The synthesis of ZSM-23 involved preparation of two mixtures. The first mixture comprised 60 g of Ludox HS-40 diluted with 126.7 g of water. In

Table 1
Characterization of zeolite samples

	ZSM-23	MTT Si	MTT Si-F
Total yield per autoclave (g)	5.4	5.4	5.8
Weight core[a] (g)	–	4.2	4.1
Weight overgrowth[b] (g)	–	1.2	1.7
Weight gain (%)	–	30	41
Overgrowth layer thickness[c] (nm)	–	22	30
Micropore volume (ml/g)	0.09	0.10	0.083
BET surface area (m^2/g)	28	24	40
Bulk Si/Al ratio (NMR)	58	66	87
Surface Si/Al ratio (XPS)	38	217	244
Al/(Si + Al) (NMR)	0.0169	0.0149	0.0114
Al/(Si + Al) (XPS)	0.026	0.0046	0.0041

[a] Estimated from amount of initial gel used and yield of crystals in initial gel.

[b] Weight overgrowth = total yield − weight core.

[c] Simplified ellipsoid model; equal growth in all directions: $V = 4/3\pi[(a) * (b) * (c)]$. $a = 1000$ nm; $b = 500$ nm; $c = 100$ nm.

the second mixture, 193.34 g of water, 0.87 g of Na-aluminate, 4.88 g of NaOH, 3.60 g of H_2SO_4, and 10.96 g of the diquat-7 salt were combined and mixed thoroughly. The second mixture was added to the first mixture under stirring. The resulting gel was divided over four autoclaves and heated in an oven for 72 h at 160 °C. After 72 h, the content of the four autoclaves was combined, and 1/4 of the volume was set aside. This fraction serving as ZSM-23 reference material was filtered, washed with deionized, water and dried at 60 °C. To the remaining 3/4 of the autoclave content, a second gel without aluminum was added. This gel comprised 48.34 g of H_2O, 1.22 g of NaOH, 0.9 g of H_2SO_4, and 2.74 g of diquat-7 dibromide, mixed separately and combined with 15 g of Ludox HS-40 diluted with 31.68 g of H_2O. The resulting mixture was divided into two equal parts. One of these parts was divided over two autoclaves; 1.74 g of NH_4F was added to the other part, and the resulting mixture divided over two additional autoclaves. The four autoclaves were heated for 24 h at 160 °C. After cooling, the contents were filtered, washed, and dried at 60 °C. The product resulting from the gel without NH_4F is referred to as MTT Si; the product resulting from the gel with NH_4F added, as MTT Si-F. Based on the weights of the synthesis mixtures and the zeolite product yields, estimated weight gains of 30% for MTT Si and 41% for MTT Si-F were obtained in the second step of the crystallization (Table 1).

The organic template was removed via the following procedure. The zeolite powder was loaded in a quartz tube, heated to 400 °C at a rate of 1 °C/min under a stream of nitrogen gas, and kept at 400 °C for 12 h to convert the template into carbonaceous material, as indicated the sample's black color. Through this procedure, a substantial part of the hydrogen is eliminated from the organic molecules to minimize steaming of the zeolite on calcination in the subsequent step. After cooling to 100 °C, nitrogen was substituted for oxygen gas, and the sample was heated to 550 °C for 12 h to eliminate the carbonaceous deposit.

2.2. Characterization

The XRD characterization was carried out using a Siemens D5000 diffractometer using Ni-filtered Cu-K_α radiation of 0.154187 nm at 40 kV and 50 mA. The XRD data were recorded between $2\theta = 3°$ and $60°$ at a scanning rate of $0.01°/s$. The ^{27}Al MAS NMR spectra were recorded with a Bruker Avance DRX400 spectrometer (9.4 T). A total of 12,000 scans were accumulated, with a recycle delay of 100 ms. The samples were spun at 20 kHz. A 0.1-M aqueous solution of $Al(NO_3)_3 \cdot 9H_2O$ was used to calibrate the chemical shift. XPS was performed with a SSI X-probe (SSX-100/206) spectrometer (Surface Science Instruments) working with a monochromatic Al-K_α radiation (10 kV, 22 mA). Charge compensation was achieved using an electron flood gun adjusted at 8 eV and placing a nickel grid 3.0 mm above the sample. The pass energy for the analyzer was 50 eV, and the spot size was 1000 μm in diameter, corresponding to a full width at half maximum of 1.1 eV for the Au $4f_{7/2}$ band of a gold standard.

Nitrogen physisorption isotherms at 77 K were recorded with an Omnisorp-100 analyzer (Coulter) operating in continuous-flow mode. Before the isotherms were recorded, calcined samples were evacuated at 673 K under high vacuum (10^{-6} kPa) for at least 12 h.

SEM pictures were taken on a Philips XL30 FEG apparatus. A gold film was sputtered onto the samples before their observation.

Particle size analysis was done with a Coulter light-scattering particle size analyzer. Dynamic light scattering in backscattering mode was performed using a high-performance particle size analyzer (ALV, Germany) equipped with 3-mW He–Ne laser (632.8 nm).

2.3. Catalytic experiments

The zeolite materials were ammonium-exchanged by slurrying the powders overnight in a 0.5-M NH_4Cl solution. Platinum was loaded on the sample by the incipient wetness impregnation technique using an aqueous solution of $Pt(NH_3)_4Cl_2$ to obtain a Pt loading of 0.3 wt%. The impregnated samples were dried overnight at 60 °C. The zeolite powder was shaped into pellets with diameters between 0.125 and 0.250 mm by compressing, crushing, and sieving. Then 50 mg of these pellets were charged in the parallel microreactor tubes of a high-throughput reactor unit [31]. The catalyst activation procedure involved calcination under flowing oxygen at 400 °C, followed by reduction in hydrogen at the same temperature. The feedstock for the catalytic experiments was decane (ACROS, purity >99%). The reactor was operated at a total pressure of 0.45 MPa and a hydrogen:hydrocarbon ratio of 375. The space time based on decane amounted to 2600 kg s/mol. The reaction temperature was varied in the range of 180–280 °C. Analysis of the reaction products was done on-line using a fast gas chromatograph equipped with a multicapillary column [31].

3. Results and discussion

3.1. Characterization of ZSM-23 and Si enriched MTT

XRD diagrams of calcined ZSM-23 and calcined MTT Si and MTT Si-F materials shown in Fig. 2 reveal the presence

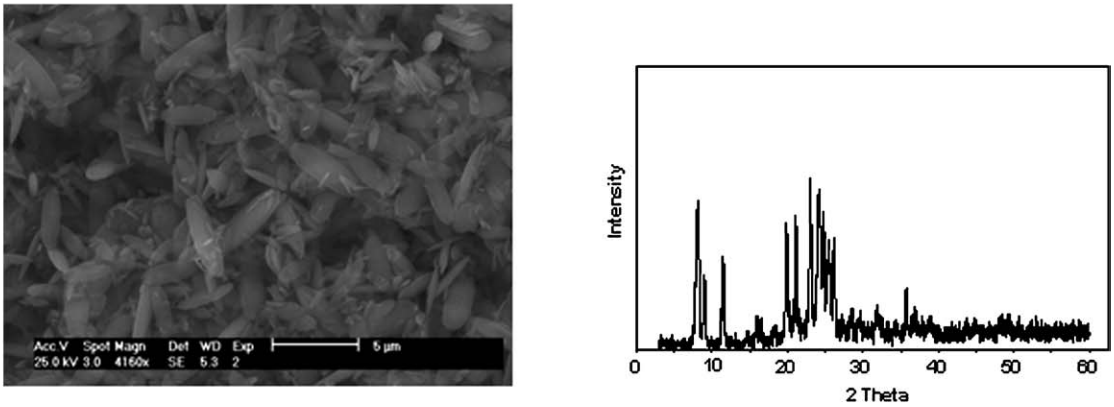

ZSM-23

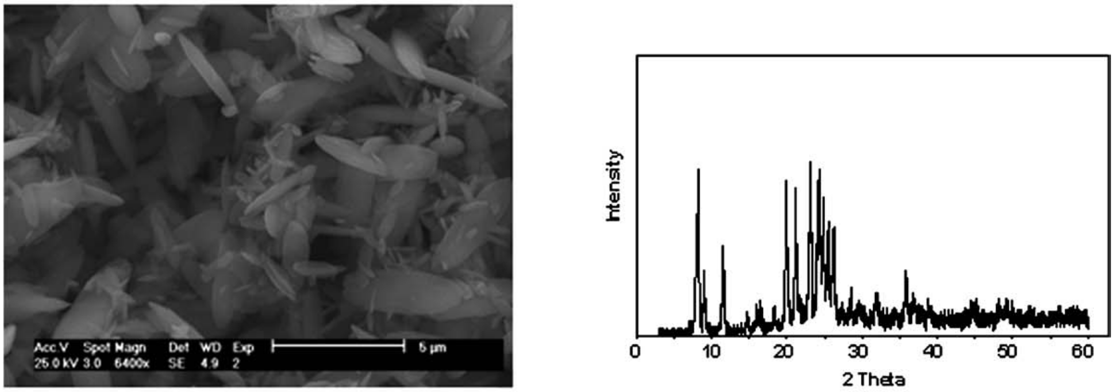

MTT Si

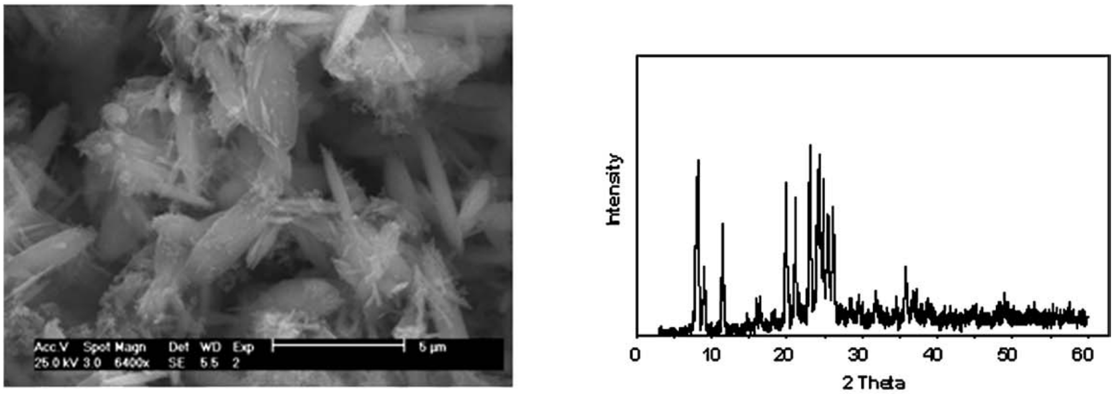

MTT Si-F

Fig. 2. SEM pictures and XRD diagrams of calcined ZSM-23 reference material, MTT Si and MTT Si-F.

of phase-pure MTT-type material [32]. The ellipsoidal shape of the ZSM-23 crystals was shown on SEM (Fig. 2). The particle size varied from 0.5 to 5 µm. This size variation suggests that crystal nucleation was spread over a broad period of the hydrothermal treatment time. The ellipsoidal particle morphology was preserved in the MTT Si and MTT Si-F samples. Assuming that all ZSM-23 particles grew uniformly during the second crystallization step in the presence of siliceous gel, the thickness of the siliceous overgrowth layer can be estimated based on the weight gain (Table 1). For crystal dimensions of 1000 × 500 × 100 nm, weight gains of 30% for MTT Si and 41% for MTT Si-F represent growth by 22 and 30 nm, respec-

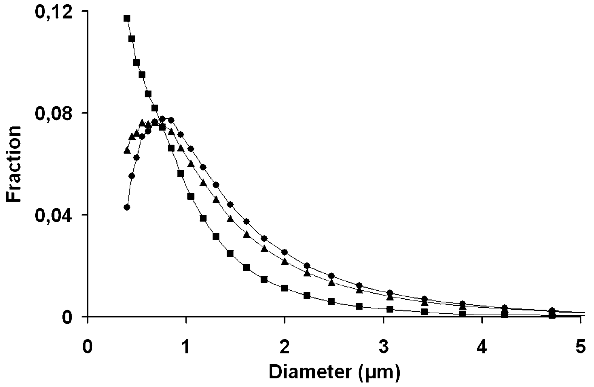

Fig. 3. Particle size distribution of ZSM-23 (■), MTT Si (●) and MTT Si-F (▲) samples determined with light scattering particle size analyzer.

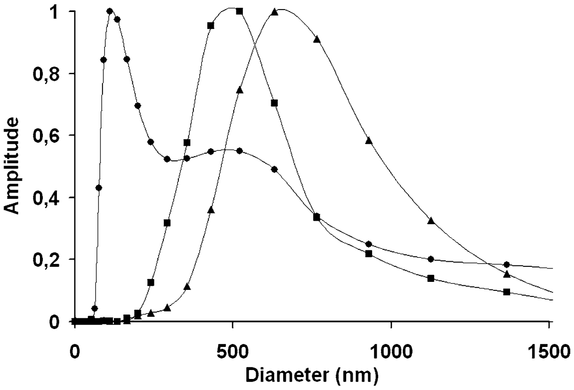

Fig. 4. Particle size distribution of the fine particle fractions of ZSM-23 (■), MTT Si (▲) and MTT Si-F (●) determined with dynamic light scattering.

tively, in every direction. According to SEM, the MTT Si and MTT Si-F materials exhibited a particle size variation similar to that of the ZSM-23 material (Fig. 2). Given the broad distribution of particle sizes, an increase in size on the order of tens of nm is difficult to observe with SEM. For the smallest crystals, growth in the long direction seemed to be more favored in the MTT Si-F material than in the ZSM-23 sample. The particle size distributions of the ZSM-23, MTT Si, and MTT Si-F samples determined by light-scattering particle size analysis are shown in Fig. 3. The lower detection limit of the instrument was ca. 0.5 µm. The samples were suspended in 0.5 M NH_4Cl solution and subjected to ultrasound treatment to disrupt aggregates before measurement. The size increase of the MTT Si and MTT Si-F samples compared with the parent ZSM-23 was obvious.

Micropore volumes determined by t-plot analysis of nitrogen adsorption isotherms (Table 1) were 0.09 ml/g on ZSM-23, 0.10 ml/g on MTM Si, and 0.08 ml/g on MTT Si-F. According to these values, the microporosities of the overgrowth layers were similar to those of the ZSM-23 core. The micropores of the ZSM-23 particle cores are accessible to nitrogen molecules. The specific external surface area of MTT Si was slightly lower than that of the ZSM-23 reference material (24 m^2/g vs. 28 m^2/g), reflecting the moderate growth of the individual crystals in the second step of the crystallization. The specific external surface area of the MTT Si-F sample was considerably larger (40 m^2/g), probably due to the formation of a fraction of very fine elongated crystals observed on SEM (Fig. 2). These very fine elongated crystals most likely nucleated during the second step of the synthesis and presumably are devoid of aluminum. The fine particle fractions of the zeolite samples were further investigated with dynamic light scattering. The samples were suspended in a NH_4Cl solution, treated with ultrasound, and allowed to settle overnight in the cuvette to observe the unsettled fine particles. The ZSM-23 and MTT Si samples contained particles measuring ca. 500 and 700 nm, respectively (Fig. 4), smaller particles were absent. This finding indicates that the finest fraction underwent particle growth in the second step of the synthesis. The MTT Si-F sample had very fine particles measuring ca. 100 nm next to 500-nm particles. The secondary nucleation already hinted at in the SEM observations was confirmed with dynamic light scattering.

The calcined ZSM-23, MTT Si, and MTT Si-F samples were characterized with ^{27}Al MAS NMR. All aluminum was in tetrahedral coordination. The Si/Al ratio of the bulk of the samples was determined from the intensity of the ^{27}Al MAS NMR signal and comparison with a ZSM-23 sample of known chemical composition. The Si/Al ratio of the ZSM-23 sample serving as core for the silicon-enriched samples was 58. The bulk Si/Al ratio was 66 in the MTT Si sample and 87 in the MTT Si-F sample, confirming silicon enrichment in the second step of the crystallization. Ascribing the weight gain in the second step of the synthesis entirely to silicon, and assuming that the core of the crystals had an Si/Al ratio of 58, bulk Si/Al ratios of 75 and 83 would be expected for the MTT Si and MTT Si-F samples, respectively (Table 1). The actual bulk Si/Al values of 66 and 87 are close to those estimated for such a model. The chemical composition of the external surface of the crystals was probed with XPS. The analysis dept of the XPS technique is on the order of a few nm but inevitably <10 nm. The ZSM-23 sample had a surface Si/Al ratio of 38, compared with 58 for the bulk. In many high-silica zeolites, Si uptake is favored over Al uptake, which is postponed to the end of crystal growth, at which point Al uptake is forced in the presence of an increased concentration in the mother liquor. The Si/Al ratio was 217 on the surface of the MTT Si sample and 244 on the surface of the MTT Si-F sample. These high values reveal that the ZSM-23 cores were systematically covered with a siliceous overlayer. Isomorphic substitution of Si with Al gives rise to a negative framework charge and an acid site when compensated with a proton. Provided that each Al atom gives rise to an acid site, the acid site concentration is given by the Al/(Al + Si) atomic ratio. The Al/(Al + Si) ratios were 0.026 on the surface of ZSM-23, 0.0046 on the surface of MTT Si, and 0.0041 on the surface of MTT Si-F. The acid site concentration on the crystal surface was six times lower in the overgrown materials than in the ZSM-23 reference sample. The highest surface Si/Al ratio of 244 was obtained when NH_4F was added (sample MTT Si-F). These observations closely match the fact that fluoride is a complexing agent for aluminum that blocks aluminum uptake into the growing zeolite crystals.

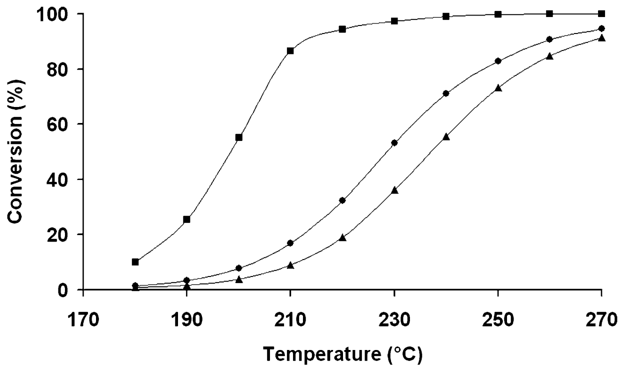

Fig. 5. Conversion of *n*-decane with increasing temperature over Pt/H-ZSM-23 (■), Pt/H-MTT Si (●) and Pt/H-MTT Si-F (▲).

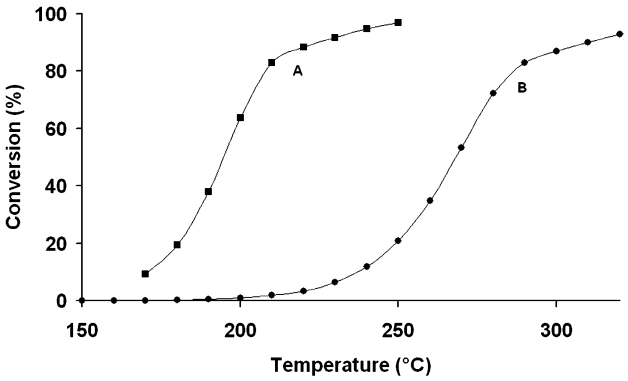

Fig. 6. Simulation of the conversion of decane in tubular packed-bed reactor according to the microkinetic model for pore mouth and key–lock catalysis on Pt/H-ZSM-22 [32]. The number of pore mouths was 340 µmol/kg (A) and 3.4 µmol/kg (B).

3.2. *Catalytic evaluation*

The conversion of decane over the three zeolites converted into bifunctional catalysts is plotted against reaction temperature in Fig. 5. The Pt/H-ZSM-23 zeolite converted decane at lower temperatures than the samples with silicate overgrowth. At 200 °C and a contact time of 2600 kg s/mol, decane conversion was 56% on Pt/H-ZSM-23, 7% on Pt/H-MTT Si, and 4% on Pt/H-MTT Si-F. Assuming that under these conditions the reactor operates under differential conditions, the apparent reaction rates of decane conversion were 350 µmol/(kg s) on Pt/H-ZSM-23, 44 µmol/(kg s) on Pt/H-MTT Si, and 26 µmol/(kg s) on Pt/H-MTT Si-F. Under ideal conditions of bifunctional catalysis, the rate-limiting step of the reaction scheme is located on the acid sites [33]. The bulk Al/(Si + Al) ratios of the three samples differed only slightly: 0.0169, 0.0149, and 0.0114, respectively (Table 1). The significant activity differences cannot be explained by these small differences in overall Al fractions. The activity differences were in better agreement with differences of the Al/(Al + Si) ratios at the crystal surfaces determined with XPS (Table 1). Assuming that each Al generated an acid site, as suggested by the ^{27}Al MAS NMR data, MTT Si had a sixfold-lower acid site concentration at its surface and an eightfold-lower catalytic activity than the ZSM-23 reference material. Along with the compositional differences at the crystal surfaces, the lower concentration of pore mouths in MTT Si compared with ZSM-23 revealed by the smaller specific external surface area (24 m^2/g vs. 28 m^2/g) also contributed to the difference. The MTT Si-F sample had a higher specific external surface area (i.e., 40 m^2/g), due to the presence of a fraction of very fine but catalytically inactive zeolite particles with purely siliceous composition, as discussed earlier.

The slope of the decane conversion curve against temperature was smaller on Pt/H-MTT Si and Pt/H-MTT Si-F than on Pt/H-ZSM-23 (Fig. 5), indicating lower apparent activation energy. In principle, lower apparent activation energies can be associated with intracrystalline diffusion becoming rate-determining or with decreased surface coverage of the reactive intermediate at increasing temperature [34,35]. In pore mouth catalysis, isomerization reactions occur at the external surface of the zeolite crystals, and intracrystalline diffusion limitations are not expected to play a role. Provided that pore mouth catalysis is operative, adsorption should be responsible for the observed decrease in apparent activation energy with reaction temperature. The impact of temperature on decane conversion according to pore mouth and key–lock catalysis can be illustrated with a related catalyst, Pt/H-ZSM-22, for which a single-event microkinetic model of decane isomerization and hydrocracking has been developed [8].

The Pt/H-ZSM-22 model was run to evaluate the affect of eliminating active sites from pore mouths and bridges on decane conversion (Fig. 6). Two catalysts were considered: one with 340 µmol active sites per kg catalyst evenly distributed over pore mouths and bridges, and one with 100 times fewer sites. The catalyst with the fewest sites required higher temperatures to realize decane conversion, as expected, but also presented a less steep curve of conversion against temperature, tantamount to a lower apparent activation energy. In the detailed adsorption and reaction scheme on which the model is based, a hydrocarbon molecule is physisorbed according to different modes, each with a specific adsorption enthalpy and entropy depending on the penetration of alkyl groups into the pore mouth [36]. Experimental adsorption isotherms of individual *n*- and iso-alkanes were modeled by additivity considering that atoms inside the pore mouth are subjected to stronger force fields than atoms of the hydrocarbon remaining outside the pore. This model was used to estimate coverage of the acid sites in the conversion of decane on the ZSM-22 catalysts with the different acid site concentrations (Fig. 7). Under reaction conditions, saturation of the adsorption capacity occurred; only at temperatures exceeding 300 °C was a small fraction of adsorption sites vacated. The reaction was of zero order in decane. An important observation was the change in adsorption mode of the hydrocarbon from pore mouth to key–lock with increasing temperature (Fig. 7). Below 200 °C, molecules adsorbed with one alkyl chain into a pore (pore mouth). Above 200 °C, the adsorption mode was altered, and an increasing number of molecules were found on the bridges between pore openings. With increasing temperature, adsorption modes involving the highest entropy losses (i.e., those involving penetration of a large part

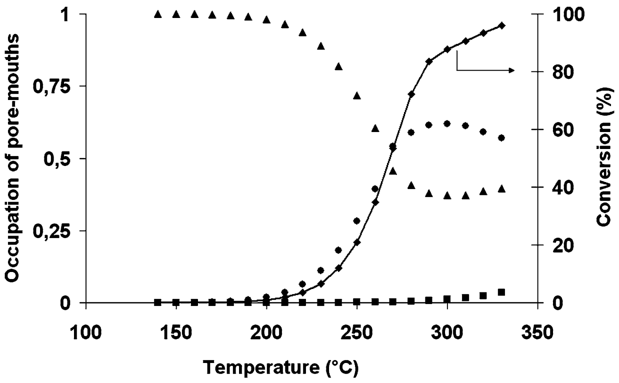

Fig. 7. Simulation of decane conversion (◆) and of the occupation of pore mouths by alkanes adsorbed according to pore mouth (▲) and key–lock modes (●) and of the fraction of empty pore mouths (■) on Pt/H-ZSM-22 with 3.4 µmol/kg of pore mouths.

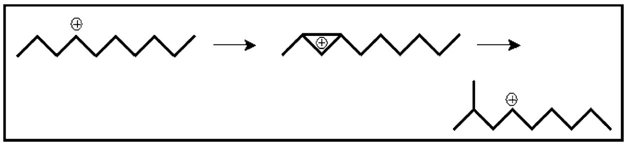

Scheme 1. The conversion of n-decane into monobranched isomers.

of the carbon chain into the pore for thermodynamic reasons) were disfavored.

The decrease in apparent activation energy on introduction of a siliceous rim in the MTT zeolite can be explained as a temperature effect in the following way. The conversion of n-decane into monobranched isomers proceeds via protonated cyclopropane intermediates transforming a secondary into a secondary alkylcarbenium ion, as shown in Scheme 1.

This reaction can occur both in pore mouths and on bridge sites. At lower temperatures, this reaction occurs preferentially at pore mouth sites, and consecutive reactions are limited due to sterical hindrance. At higher temperatures, however, the contribution of bridge acid sites to n-decane conversion becomes more important, and hence consecutive isomerization and cracking reactions involving tertiary alkylcarbenium ions gain importance. The tendency of the molecules to adsorb on the bridges rather than in the pore mouths (Fig. 7) can explain the flattening of the onset of the conversion curve at the high reaction temperatures under which the catalysts with siliceous rims were tested. In the kinetic model, it is assumed that only secondary alkylcarbenium ions can be formed in pore mouths. Because of sterical limitations, formation of tertiary alkylcarbenium ions in pore mouths is not allowed (Fig. 1). In the key–lock adsorption modes involving acid sites on the bridges between pore mouths, tertiary alkylcarbenium ion formation is allowed (Fig. 1). Once the hydrocarbon chain is branched, reactions involving tertiary alkylcarbenium ions are possible. The apparent activation energy is the sum of, among other factors, the true activation energy and the protonation enthalpy. The protonation energy leading to tertiary alkylcarbenium ions is 40–45 kJ/mol lower than that for secondary alkylcarbenium ions [37]. Consequently, the apparent activation energy of key–lock conversions involving tertiary alkylcarbenium ions is substantially lower that for pore mouth conversions. The larger contribution of key–lock catalysis on the sample with a low number of acid sites contributes to the flattening of the decane conversion curve.

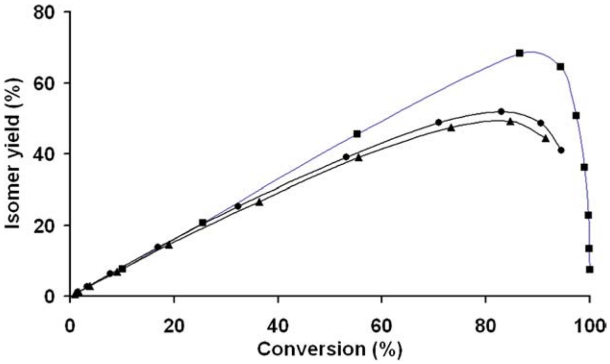

Fig. 8. Total yield of isomers with increasing conversion of n-decane with increasing temperature over Pt/H-ZSM-23 reference material (■), Pt/H-MTT Si (●) and Pt/H-MTT Si-F (▲).

The flattening of the conversion versus temperature curves at high conversions (i.e., $>80\%$ conversion) is related to the fact that the equilibrium between n-decane and its isomers is approached at these conversions. Further reaction is possible only through cracking reactions. When only secondary alkylcarbenium ions are involved, cracking rate coefficients are lower than isomerization rates [38]. This leads to the pronounced flattening of curve A in Fig. 6 irrespective of activation energy. When tertiary alkylcarbenium ions are involved, isomerization and cracking rate coefficients are more or less on the same order of magnitude, and the flattening of the conversion versus temperature curve is less pronounced (cf. curve B in Fig. 6).

The yield of skeletal isomers from decane conversion is plotted against decane conversion in Fig. 8. On Pt/H-ZSM-23, the isomer yield attained a maximum of 70%. On the zeolite with siliceous surface, a lower maximum yield of isomers of only around 50% was obtained. Hydrocracking is sterically suppressed on tubular, medium-pore zeolites. On Pt/H-ZSM-22 at low temperatures, the main contribution stems from β-scission reactions involving secondary alkylcarbenium ions in pore mouth adsorption modes [7]. The temperature effect on the isomer yields can be explained if the adsorption mode is shifted from pore mouth to key–lock. In the key–lock mode, β-scission reactions involving both secondary and tertiary alkylcarbenium ions are allowed [8], limiting the isomerization yield. In previous work with Pt/H-ZSM-22 catalyst, decreased skeletal isomerization yield was observed when decane isomerization was performed at higher temperatures [39].

The distribution of individual skeletal isomers obtained over the three catalysts was investigated. Particularly relevant to the present discussion is the content of 2-methylnonane and 5-methylnonane in the methylnonane product fraction (Table 2). 2- and 3-methylnonane are typical reaction products from pore mouth catalysis, whereas 4- and especially 5-methylnonane are formed via key–lock catalysis [12,13]. The Pt/H-ZSM-23 catalyst shows higher preference for 2-methylnonane than the Si overgrown samples, which slightly favor 4-

Table 2
Distribution of monomethylbranched isomers of decane

	ZSM-23	MTT Si	MTT Si-F
10% isomerization yield			
2-methylnonane (%)	54.1	51.3	51.1
3-methylnonane (%)	27.9	27.8	27.9
4-methylnonane (%)	10.2	12.1	12.0
5-methylnonane (%)	7.8	8.8	9.0
30% isomerization yield			
2-methylnonane (%)	53.3	49.9	49.8
3-methylnonane (%)	28.0	28.1	27.9
4-methylnonane (%)	10.8	13.1	13.1
5-methylnonane (%)	7.9	8.9	8.9

and 5-methylnonane. This change in methyl branching pattern is ascribed to the different temperature windows in which the samples were active (Fig. 5). The low temperatures at which Pt/H-ZSM-23 was investigated favor pore mouth catalysis and 2-methylnonane formation; the high temperatures at which Pt/H-MTT Si and Pt/H-MTT Si-F were tested favor the key–lock mode and 4- and 5-methylnonane formation. In previous work [40], differently synthesized ZSM-23 samples were compared as catalysts for octadecane isomerization and found to have similar catalytic activity. They displayed almost identical skeletal isomer distributions, characteristic of this zeolite type. It can be concluded that ZSM-23 and the overgrowths have the same type of pore mouth and key–lock sites, and that the difference in active temperature window causes the selectivity differences.

The yield of hydrocracked products according to carbon numbers and the content of linear and branched products in the carbon number fractions at 35% cracking conversion are reported in Fig. 9. The cracking patterns on Pt/H-ZSM-23 and Pt/H-MTT Si differed substantially. Higher amounts of C_2, C_3, and C_7 were obtained on the reference material. Pt/H-MTT Si favored central cracking. Pt/H-ZSM-23 yielded high amounts of linear cracking products in the different carbon number fractions, whereas on Pt/H-MTT Si and Pt/H-MTT Si-F, the formation of branched cracked products was favored. Differences in cracking behavior are expected, because the relative contributions of the different cracking modes are strongly temperature dependent [8,36].

4. Conclusion

MTT zeolites with compositional variation inside individual crystals (MTT Si) were synthesized. The cores of these crystals contain silicon and most of the aluminum. The concentration of aluminum and acid sites on the surface was about six times lower in the MTT Si samples than in reference ZSM-23 zeolite. The catalytic activity of MTT-type zeolites can be correlated with the acid site concentration on the surface of the crystals rather than in the bulk. The samples with siliceous rims had lower apparent activation energy than the ZSM-23 core material. Kinetic models revealed that was due to the high reaction temperatures at which these MTT-Si materials were catalytically evaluated. At higher temperatures, physisorption on key–lock sites was favored over pore mouth sites. The introduction of the first methyl branching occurred in pore mouths rather than on bridge sites. The shortness of suitably adsorbed molecules in more mouths explains the flattening of the decane conversion curve. The availability of a more extensive reaction network involving tertiary next to secondary alkylcarbenium ions on bridge sites also caused a decrease in apparent activation energy. The enhanced relative contribution of key–lock with respect to pore mouth catalysis was evident from the distribution of methylnonane reaction products, particularly the formation of 2 vs. 4- and 5-methylnonane, as well as from the

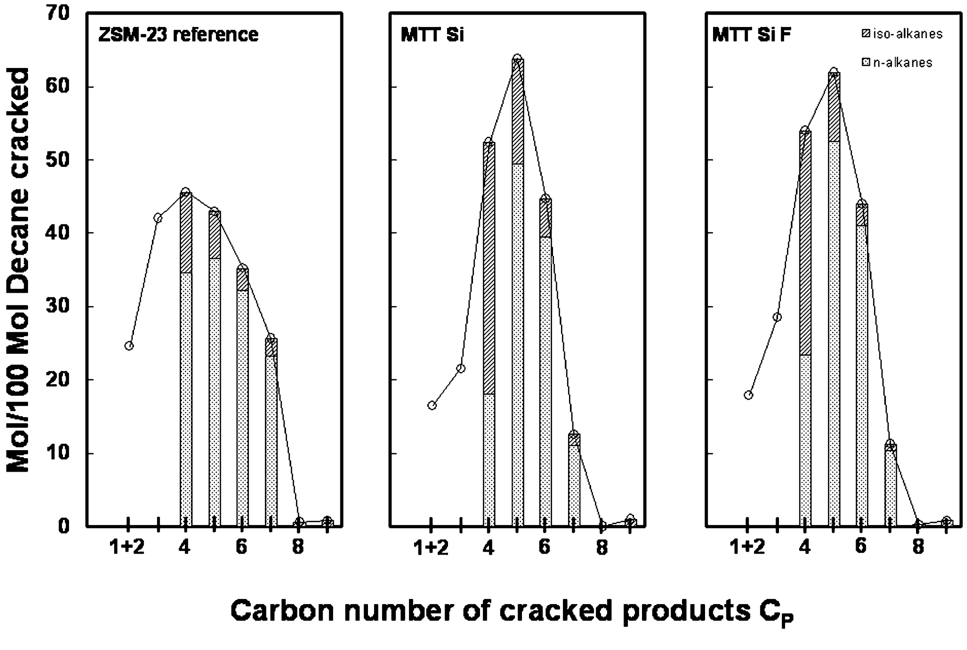

Fig. 9. Distribution of the hydrocracked products from n-decane over 0.3Pt/H-ZSM-23 reference material, Pt/H-MTT Si and Pt/H-MTT Si-F at 35% cracking conversion.

branching degree of the cracked products, which was high on the MTT Si catalysts.

Acknowledgments

W.H. and J.F.M.D. acknowledge IWT and FWO-Vlaanderen for doctoral and postdoctoral fellowships, respectively. K.J.H., J.A.M., and P.A.J. acknowledge the Flemish government for supporting a concerted research action (GOA). The involved teams participate in the IAP-PAI program [SC]^2 sponsored by the Belgian government. The authors thank the referees for valuable suggestions.

References

[1] I.E. Maxwell, W.H.J. Stork, in: H. Bekkum, E.M. Flanigen, J.C. Jansen (Eds.), Introduction to Zeolite Science and Practice, vol. 58, Elsevier, Amsterdam, 1991, p. 571.
[2] S. Ernst, J. Weitkamp, J.A. Martens, P.A. Jacobs, Appl. Catal. 48 (1989) 137.
[3] V.T. Nghiem, G. Sapaly, P. Mériaudeau, C. Naccache, Top. Catal. 14 (2001) 131.
[4] E.B. Webb, G.S. Grest, Catal. Lett. 56 (1998) 95.
[5] T.L.M. Maesen, M. Schenk, T.J.H. Vlugt, J.P. de Jonge, B. Smit, J. Catal. 188 (1999) 403.
[6] J.A. Martens, W. Souverijns, W. Verrelst, R. Parton, G.F. Froment, P.A. Jacobs, Angew. Chem. Int. Ed. 34 (1995) 2528.
[7] C.S.L. Narasimhan, J.W. Thybaut, G.B. Marin, P.A. Jacobs, J.A. Martens, J.F. Denayer, G.V. Baron, J. Catal. 220 (2003) 399.
[8] C.S.L. Narasimhan, J.W. Thybaut, G.B. Marin, J.F. Denayer, G.V. Baron, J.A. Martens, P.A. Jacobs, Chem. Eng. Sci. 59 (2004) 4765.
[9] J.F. Denayer, G.V. Baron, J.A. Martens, P.A. Jacobs, J. Phys. Chem. B 102 (1998) 3077.
[10] J.F. Denayer, W. Souverijns, P.A. Jacobs, J.A. Martens, G.V. Baron, J. Phys. Chem. B 102 (1998) 4597.
[11] R.A. Ocakoglu, J.F.M. Denayer, G.B. Marin, J.A. Martens, G.V. Baron, J. Phys. Chem. B 107 (2003) 398.
[12] M.C. Claude, J.A. Martens, J. Catal. 190 (2000) 39.
[13] M.C. Claude, G. Vanbutsele, J.A. Martens, J. Catal. 203 (2001) 213.
[14] J.F. Denayer, G.V. Baron, G. Vanbutsele, P.A. Jacobs, J.A. Martens, Chem. Eng. Sci. 54 (1999) 3553.
[15] P.B. Weisz, V.J. Frilette, J. Phys. Chem. 64 (1960) 382.
[16] S.M. Csicsery, Pure Appl. Chem. 58 (1986) 841.
[17] T.F. Degnan, J. Catal. 216 (2003) 32.
[18] E.G. Derouane, J. Catal. 100 (1986) 541.
[19] D. Farcasiu, J. Hutchison, L. Li, J. Catal. 122 (1990) 34.
[20] C.S.H. Chen, R.F. Bridger, J. Catal. 161 (1996) 687.
[21] R.W. Weber, K.P. Möller, M. Unger, C.T. O'Connor, Microporous Mesoporous Mater. 23 (1998) 179.
[22] G.P. Handreck, T.D. Smith, Zeolites 10 (1990) 746.
[23] R. Szostak, in: H. Bekkum, E.M. Flanigen, J.C.Jansen (Eds.), Introduction to Zeolite Science and Practice, vol. 58, Elsevier, Amsterdam, 1991, p. 153.
[24] C. Berger, A. Raichle, R.A. Rakoczy, Y. Traa, J. Weitkamp, Microporous Mesoporous Mater. 59 (2003) 1.
[25] R. von Ballmoos, W.M. Meier, Nature 289 (1981) 782.
[26] E.G. Derouane, J.P. Gilson, Z. Gabelica, C. Moustydesbuquoit, J. Verbist, J. Catal. 71 (1981) 447.
[27] Q. Li, Z. Wang, J. Hedlund, D. Creaser, H. Zhang, X. Zou, A.J. Bons, Microporous Mesoporous Mater. 78 (2005) 1.
[28] C.S. Lee, T.J. Park, W.Y. Lee, Appl. Catal. A 96 (1993) 151.
[29] G. Sastre, A. Chica, A. Corma, J. Catal. 195 (2000) 227.
[30] E.W. Valyocsik, US Patent 4 490 342 (1984), to Mobil Oil Corporation.
[31] W. Huybrechts, J. Mijoin, P.A. Jacobs, J.A. Martens, Appl. Catal. A 243 (2001) 1.
[32] Ch. Baerlocher, W.M. Meier, D.H. Olson, Atlas of Zeolite Framework Types, Elsevier, Amsterdam, 2001.
[33] J.W. Thybaut, C.S.L. Narasimhan, J.F.M. Denayer, G.V. Baron, P.A. Jacobs, J.A. Martens, G.B. Marin, Ind. Eng. Chem. Res. 44 (2005) 5159.
[34] G.W. Roberts, H.H. Lamb, J. Catal. 154 (1995) 364.
[35] G.F. Froment, K.B. Bischoff, Chemical Reactor Analysis and Design, Wiley, New York, 1990, p. 70.
[36] C.S. Laxmi Narasimhan, J.W. Thybaut, G.B. Marin, J.A. Martens, J.F. Denayer, G.V. Baron, J. Catal. 218 (2003) 135.
[37] G.G. Martens, G.B. Marin, J.A. Martens, P.A. Jacobs, G.V. Baron, J. Catal. 195 (2000) 252.
[38] J.W. Thybaut, G.B. Marin, G.V. Baron, P.A. Jacobs, J.A. Martens, J. Catal. 202 (2001) 324.
[39] J.A. Martens, R. Parton, L. Uytterhoeven, P.A. Jacobs, Appl. Catal. A 76 (1991) 95.
[40] W. Huybrechts, G. Vanbutsele, K.J. Houthoofd, F. Bertinchamps, C.S.L. Narasimhan, E.M. Gaigneaux, J.W. Thybaut, G.B. Marin, J.F.M. Denayer, G.V. Baron, P.A. Jacobs, J.A. Martens, Catal. Lett. 100 (2005) 235.